

Ultracold atomic absorption imaging system in high magnetic fields

Yuying Chen(陈玉莹), Zhengxi Zhang(张正熙), Hongmian Shui(税鸿冕), Yun Liang(梁芸), Fansu Wei(魏凡粟), and Xiaoji Zhou(周小计)

Citation: Chin. Phys. B, 2025, 34 (**5**): 053303. DOI: 10.1088/1674-1056/adc7f6
http://cpb.iphy.ac.cn; http://iopscience.iop.org/cpb

What follows is a list of articles you may be interested in

Femtosecond mode-locking and soliton molecule generation based on a GaAs saturable absorber

Chen-Yan Zhang(张辰妍), Xin-He Dou(窦鑫河), Zhen Chen(陈震), Jing-Han Zhao(赵靖涵), Wei Sun(孙薇), Ze-Yu Fan(樊泽宇), Tao Zhang(张涛), Hao Teng(滕浩), and Zhi-Guo Lv(吕志国)
Chin. Phys. B, 2025, 34 (**1**): 014205. DOI: 10.1088/1674-1056/ad8db3

Enhanced picosecond terahertz wave generation based on cascade effects in a terahertz parametric generator

Jingxi Zhang(张敬喜), Yuye Wang(王与烨), Bingfeng Xu(徐炳烽), Kai Chen(陈锴), Zikun Liu(刘紫鲲), Hongru Ma(马鸿儒), Degang Xu(徐德刚), and Jianquan Yao(姚建铨)
Chin. Phys. B, 2024, 33 (**8**): 084203. DOI: 10.1088/1674-1056/ad47b0

Gigahertz frequency hopping in an optical phase-locked loop for Raman lasers

Dekai Mao(毛德凯), Hongmian Shui(税鸿冕), Guoling Yin(殷国玲), Peng Peng(彭鹏), Chunwei Wang(王春唯), and Xiaoji Zhou(周小计)
Chin. Phys. B, 2024, 33 (**2**): 024209. DOI: 10.1088/1674-1056/ad174b

Manganese dioxide as wide adaptive ultrafast photonic device for pulsed laser generation

Xin-He Dou(窦鑫河), Zhen Chen(陈震), Chen-Yan Zhang(张辰妍), Xiang Li(李响), Fei-Hong Qiao(乔飞鸿), Bo-Le Song(宋博乐), Shan Wang(王珊), Hao Teng(滕浩), and Zhi-Guo Lv(吕志国)
Chin. Phys. B, 2024, 33 (**11**): 114202. DOI: 10.1088/1674-1056/ad71b5

Finesse measurement for high-power optical enhancement cavity

Xin-Yi Lu(陆心怡), Xing Liu(柳兴), Qi-Li Tian(田其立), Huan Wang(王焕), Jia-Jun Wang(汪嘉俊), and Li-Xin Yan(颜立新)
Chin. Phys. B, 2024, 33 (**1**): 014205. DOI: 10.1088/1674-1056/acd8ad

---

Ultracold atomic absorption imaging system in high magnetic fields

Yuying Chen(陈玉莹)[1], Zhengxi Zhang(张正熙)[2], Hongmian Shui(税鸿冕)[2,3,†], Yun Liang(梁芸)[2], Fansu Wei(魏凡粟)[2,‡], and Xiaoji Zhou(周小计)[2,3,§]

[1] *School of Physics and Electronics Engineering, Shanxi University, Taiyuan* 030006, *China*
[2] *State Key Laboratory of Photonics and Communications, School of Electronics, Peking University, Beijing* 100871, *China*
[3] *Institute of Carbon-based Thin Film Electronics, Peking University, Taiyuan* 030012, *China*

(Received 24 February 2025; revised manuscript received 28 March 2025; accepted manuscript online 2 April 2025)

Absorption imaging is a fundamental technique for quantitatively extracting information from ultracold atom experiments. Since ultracold ^{6}Li atoms are prepared and detected under high magnetic fields, the suitable detuning of the probe light can reach the GHz level compared to zero-field imaging. Therefore, based on the energy level structure of ^{6}Li atoms and the requirements of subsequent experiments, we design a high-field imaging system with a large frequency range and good robustness, starting from the rationality of the optical layout design and employing offset locking techniques. This imaging system covers the entire crossover region from Bose–Einstein condensate to Bardeen–Cooper–Schrieffer (BEC–BCS) and realizes free switching between zero-field and high-field imaging. Additionally, by introducing a proportionality coefficient to correct for the intensity fluctuations of the probe light, we mitigate its disturbance on the statistical measurement of particle numbers in the experiment. This work not only provides a design reference for other quantum gas experiments requiring absorption imaging under strong bias magnetic fields, but also serves as an important reference for improving the imaging performance.

Keywords: absorption imaging, high field imaging, offset locking, light intensity correction

PACS: 33.55.+b, 42.60.–V, 42.30.–d

DOI: 10.1088/1674-1056/adc7f6 **CSTR:** 32038.14.CPB.adc7f6

1. Introduction

Ultracold atom experiments provide an excellent platform for studying quantum many-body physics. In these experiments, the density and momentum distribution of atoms in real space and momentum space can typically be measured by direct imaging after a certain time of flight (TOF).[1,2] Many novel phenomena have been observed, including the bimodal distribution of the Bose–Einstein condensation,[3] superfluidity in optical lattice systems,[4] applications in precision measurements,[5,6] etc. Absorption imaging is the most commonly used technique for observing these phenomena, especially when measuring density distributions.[7] According to the Beer–Lambert law, the light transmittance decreases exponentially with increasing atomic density. By obtaining the light signal, the atomic density distribution can be derived.[8,9]

Magnetic fields play an important role in cold atom experiments, especially in experiments involving tunable interactions. We can adjust the Feshbach resonance magnetic field to change the corresponding scattering length,[10,11] where the energy of the scattering state coincides with the bound molecular state in the near channel. This capability has paved the way for new fields of study, including strongly interacting Fermi gases in the Bose–Einstein condensate to Bardeen–Cooper–Schrieffer (BEC–BCS) crossover,[12] Feshbach dimers,[13–15] quench dynamics,[16] etc. Absorption imaging relies on the interaction of near-resonant light with atoms in an ideal closed optical loop scheme.[9] So it is very sensitive to the energy structure of atoms, which is strongly influenced by the magnetic field. Due to level crossings and the decoupling of hyperfine level degeneracies, absorption imaging results under non-zero magnetic fields may be significantly different from those under zero magnetic fields, due to low pumping efficiency and changes in the dipole moment. Compared with previous research reports on absorption imaging systems in non-zero magnetic fields, it mainly focuses on the calibration of imaging under low magnetic field,[17,18] the selection of detection light conditions under high magnetic field[19] and the detection of the impact of light intensity on specific experimental studies.[20–23]

In this paper, we design a high-field imaging system with a large frequency range and good robustness, taking into account the energy level structure of ^{6}Li atoms and the requirements of subsequent experiments. The entire high-field imaging system is based on optical phase-locked loop offset locking technology,[24,25] combining optical layout and electrical circuit designs, achieving free switching between zero-field and high-field imaging, and enabling continuous imaging under different magnetic fields. In addition, by correcting the

†Corresponding author. E-mail: shuihongmian@163.com
‡Corresponding author. E-mail: wfs@pku.edu.cn
§Corresponding author. E-mail: xjzhou@pku.edu.cn

© 2025 Chinese Physical Society and IOP Publishing Ltd. All rights, including for text and data mining, AI training, and similar technologies, are reserved.

intensity fluctuations of the probe light in absorption imaging, we mitigate the associated noise disturbance and provide reliable data support for strong interaction experiments. Therefore, this work not only offers a reference for the design of absorption imaging systems in quantum gas experiments under strong bias magnetic fields but also enhances the reliability of experimental data through the correction of imaging light intensity under a uniform background.

2. Principle

2.1. Zeeman level splitting

In magnetic fields, the energy levels of atoms undergo splitting, a phenomenon known as the Zeeman effect. ^{6}Li has a single valence electron, resulting in a relatively simple energy level structure. Its total electron spin is $s = 1/2$, hence the ground state of ^{6}Li is $2S_{1/2}$. On the D2 line, we drive a dipole transition ($\Delta J = 1$) to the excited state $2P_{3/2}$. On the D1 line, the energy splitting of the excited state $2P_{1/2}$ is approximately 10.0528 GHz, thus the D1 and D2 transitions do not overlap, as shown in Fig. 1(a). When considering the hyperfine coupling of the nuclear spin $I = 1$ with the total angular momentum $\boldsymbol{J} = \boldsymbol{S} + \boldsymbol{L}$, the situation becomes more complex. In the absence of a magnetic field, the ground state $2S_{1/2}$ splits into two hyperfine states with total angular momentum $F = \{1/2, 3/2\}$. The splitting between these two substates is approximately $\Delta E_{\rm HF}^{\rm GS} = 228.2$ MHz $\approx 39\Gamma$ (the natural linewidth $\Gamma = 5.87$ MHz). This splitting is significantly larger than the hyperfine splitting of the excited state $2P_{3/2}$. The excited state splits into three substates with total angular momentum $F = \{1/2, 3/2, 5/2\}$, and the total energy splitting is $\Delta E_{\rm HF}^{\rm ES} = 4.6$ MHz $< \Gamma$, which is smaller than the natural linewidth Γ. Each hyperfine substate has $(2F+1)$ different m_F Zeeman sublevels, which split when a magnetic field is applied. Therefore, when an external magnetic field is applied, the degeneracy of the hyperfine states is lifted due to the Zeeman effect. In this case, the ground state splits into six distinct orthogonal eigenstates, and the excited state splits into twelve distinct orthogonal eigenstates.

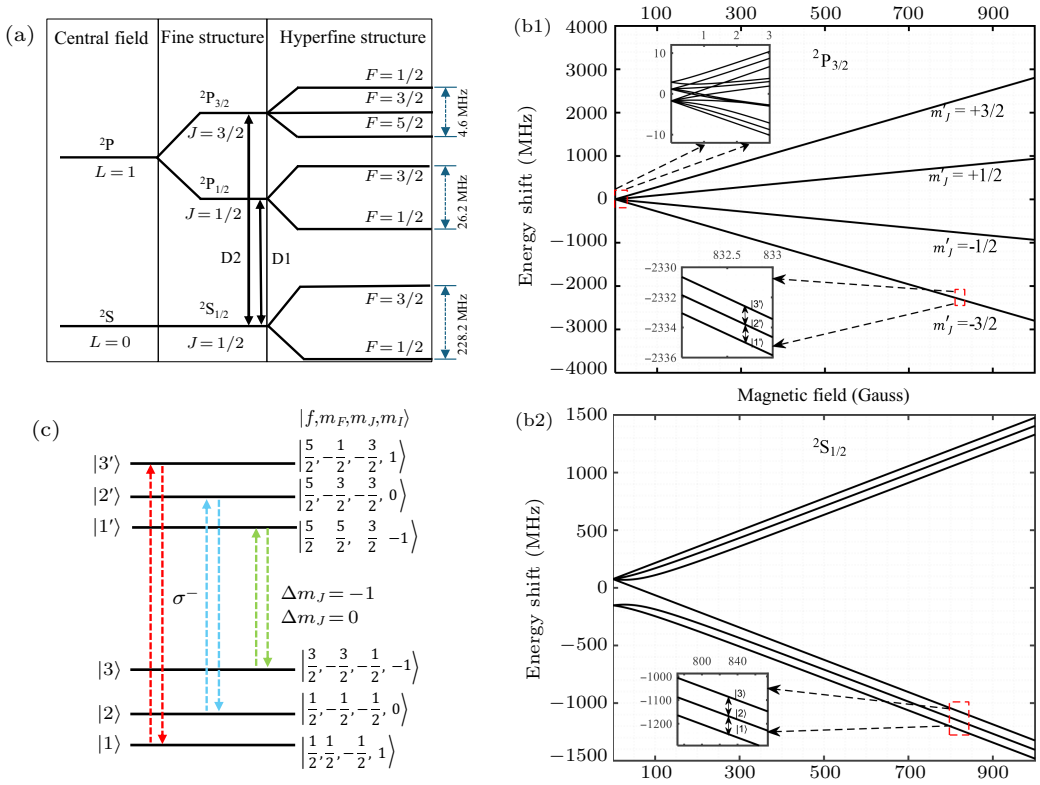


Fig. 1. Energy level diagram. (a) The level structure of the lowest levels of ^{6}Li with fine and hyperfine splitting at zero magnetic field. (b) The splitting of the different hyperfine states as a function of the magnetic field. (b1) The splitting of the $^2P_{3/2}$ level in a magnetic field. The inset in the upper left corner shows the levels splitting from the degenerate $F' = 1/2$, $F' = 3/2$, and $F' = 5/2$ manifolds. (b2) The splitting of the $^2S_{1/2}$ level in a magnetic field. The inset in the lower left corner shows the states $|1\rangle$, $|2\rangle$, and $|3\rangle$ that we typically focus on for imaging. These levels split into $m_I = -1, 0, 1$ triplets with different m_J numbers. They have $m_J = -1/2$ and $m'_J = -3/2$. (c) An enlarged view of the σ^- transition in the dipole transition under the imaging light. Given that $\Delta m_J = +1$ and $\Delta m_I = 0$, the atom can only decay from the excited state back to its initial state.

Imaging at zero magnetic field on the $|F = 1/2\rangle \rightarrow |F' = 3/2\rangle$ transition can count all atoms because the two m_F projections are degenerate. In weak magnetic fields (see the inset in the upper left corner of Fig. 1(b1)), hyperfine splitting causes us to select only one of the m_F states for imaging, which means our effective signal-to-noise ratio (SNR) is reduced. Furthermore, as the magnetic field increases, F and m_F are no longer good quantum numbers, and are replaced by m_J and m_I. As

shown in Figs. 1(b1) and 1(b2), the energy levels split into $m_I = -1, 0, 1$ triplets with different m_J numbers. We typically focus on imaging the three lowest energy states $|1\rangle$, $|2\rangle$, and $|3\rangle$ within the ground state manifold, where the ground state has $m_J = -1/2$ and $m_I = 1, 0, -1$, while the excited state uses $m'_J = -3/2$. In high magnetic fields, this transition is closed, allowing us to forgo the repump light. However, there is still a differential Zeeman shift which is approximately linear past 100 G and can be written as

$$\begin{cases} \delta_1 = -1.399\ \text{MHz/G} \cdot B + 158\ \text{MHz}, \\ \delta_2 = -1.399\ \text{MHz/G} \cdot B + 82\ \text{MHz}, \\ \delta_3 = -1.399\ \text{MHz/G} \cdot B, \end{cases} \tag{1}$$

where δ_i is the detuning of the transition $|i\rangle \to |m'_J = -3/2\rangle$ ($i = 1, 2, 3$). The energy level frequency differences between the imaging states $|1\rangle$, $|2\rangle$, and $|3\rangle$ are $\Delta\nu_{12} = 76$ MHz and $\Delta\nu_{23} = 82$ MHz. This large frequency shift requires us to have a second laser system to generate the high-field imaging light.

Additionally, the imaging light must have the correct polarization to satisfy the selection rules for dipole-allowed transitions. For ^{6}Li atoms, in high magnetic fields, the imaging light forms a closed transition from the ground state to the excited state, as shown in Fig. 1(c), where the transition from $m_J = -1/2$ to $m'_J = -3/2$ is closed. To make the particles see purely left-circularly polarized light σ^-, the light must propagate along the quantization axis of the atoms. The Helmholtz magnetic field coils designed in the experiment define the quantization axis along the vertical direction. Therefore, to allow the imaging light to effectively interact with the atoms, the high-field imaging design is best aligned along the vertical direction of the system.

2.2. Absorption imaging

As shown in Fig. 2(a), the simplified setup of the imaging design for the experimental system is presented. To obtain atomic information in multiple dimensions, charge-coupled device (CCD) cameras are placed in both the horizontal and vertical directions. The Feshbach magnetic field is generated by a pair of Helmholtz coils oriented along the z-axis. As shown in Fig. 2(b1), the system employs single-lens imaging, with a magnification of 1 when both the object distance and the image distance are twice the focal length.

According to the Beer–Lambert law for absorption imaging, the change in light intensity after passing through an atomic ensemble can be expressed as

$$I(x,y) = I_0(x,y)\, \mathrm{e}^{-OD(x,y)} \tag{2}$$

where I_0 is the light intensity before absorption, I is the light intensity after absorption, and $OD(x,y)$ is the two-dimensional optical density of the atomic ensemble, which represents the ability of the atomic ensemble to absorb light. As shown in Fig. 2(b2), traditional absorption imaging typically requires three consecutive images. The first image captures the information after the imaging light passes through the atoms, denoted as $I_{\text{atoms}}(x,y)$. The second image captures the information of the imaging light without passing through the atoms, denoted as $I_{\text{light}}(x,y)$. The third image captures the background information without the imaging light and atoms, denoted as $I_{\text{bg}}(x,y)$. Therefore, we can obtain

$$\frac{I_{\text{f}}(x,y)}{I_{\text{i}}(x,y)} = \frac{I_{\text{atoms}}(x,y) - I_{\text{bg}}(x,y)}{I_{\text{light}}(x,y) - I_{\text{bg}}(x,y)}, \tag{3}$$

where $I_{\text{i}}(x,y)$ is the initial light intensity spatial distribution, and $I_{\text{f}}(x,y)$ is the spatial distribution of the light intensity after it has passed through the sample.

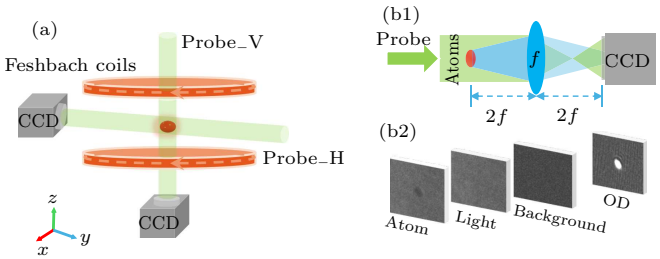


Fig. 2. Imaging system setup. (a) Simplified setup of the imaging system, where the orange coils represent a pair of Feshbach magnetic field coils, and the green beam is the imaging light. (b1) Schematic diagram of single-lens imaging, where the green beam is the imaging light, the blue represents the lens, the red is the atom cloud, and the gray indicates the CCD camera. (b2) Schematic diagram of absorption imaging, showing three typical images.

When a beam of light $I_{\text{i}}(x,y)$ is incident along the z-axis and passes through an atomic cloud, the modified Beer–Lambert law indicates that

$$\frac{\mathrm{d}I(x,y,z)}{\mathrm{d}z} = -n(x,y,z)\sigma I(x,y,z)\left(1 + \frac{I(x,y,z)}{I_{\text{sat}}}\right). \tag{4}$$

The absorption cross-section σ is defined as

$$\sigma = \frac{h\omega\Gamma}{4\pi I_{\text{sat}}} \cdot \frac{1}{1 + 4\left(\frac{\Delta}{\Gamma}\right)^2}. \tag{5}$$

Here $\Delta = \omega - \omega_0$ is the detuning between the imaging light frequency ω and the atomic resonance frequency ω_0, Γ is the spontaneous emission rate, h is the Planck constant. By measuring the laser intensity before and after the sample, the OD, which is the product of the absorption cross-section σ and the area density $n_{2\text{D}}(x,y) = \int_{-\infty}^{\infty} n(x,y,z)\,\mathrm{d}z$, can be calculated as

$$OD(x,y) = n_{2\text{D}}(x,y)\sigma = -\ln\left(\frac{I_{\text{f}}(x,y)}{I_{\text{i}}(x,y)}\right) + \frac{I_{\text{i}} - I_{\text{f}}}{I_{\text{sat}}}. \tag{6}$$

3. High-field imaging system

The imaging optical layout design is shown in Fig. 3(a). In the experiment, the two states with $F = 1/2$ are primarily used. At zero field (no bias magnetic field), the resonant absorption frequency is the center frequency of the repump. The pre-stage light undergoes a double frequency shift

of $+2 \times 258$ MHz using a 270 MHz acousto-optic modulator (AOM) (G&H 3270–195), then beats and combines with the high-field imaging light. It subsequently single passes through a 40 MHz AOM (AA Opto Electronic MTS40-A2-532.700-M002) to obtain the zero-field resonant imaging light. Since the high-field imaging light requires less power, an external cavity semiconductor laser (ECDL) is chosen as the light source. This laser uses a laser tube model HL6756MG with a maximum output power of 15 mW and negative current input, where approximately 8 mW is used for offset locking and 1 mW is used for imaging light. After the laser light is emitted, it first passes through two 30 dB isolators (ISO670-3-1.5W). It has been found that during the experiment the laser frequency can be affected by only one isolator. The D2 line laser's probe light is split into two paths here, each is combined with the semiconductor laser light. One path is used for frequency offset locking, and the other path, after a 40 MHz frequency shift, serves as a light switch for the zero-field and high-field combined beam entering the fiber. Moreover, to be able to independently control the type of probe light reaching the platform through the fiber, it must be ensured that both imaging light paths first undergo beat frequency and then imaging. The position of the light shutter is specially marked in the figure. Additionally, the polarization of the two components of light used for beat frequency locking and passing through the AOM must be unified. This model of AOM can only produce a highly efficient first-order diffracted light when the polarization is vertical linear polarization.

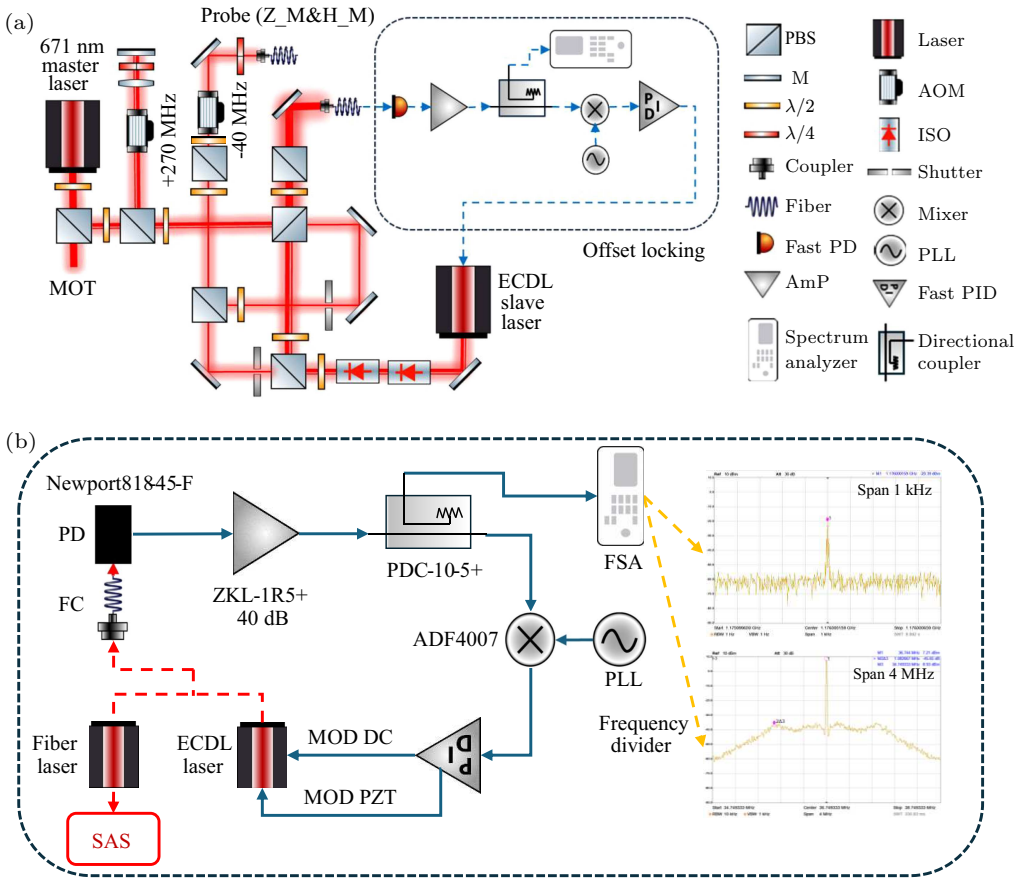


Fig. 3. (a) Schematic diagram of the high-field imaging system's pre-stage optical path design. The thin red beam represents the imaging light, the thick red beam represents the beat frequency light, and the dashed box contains a simplified diagram of the beat frequency circuit. (b) Enlarged view of the beat frequency circuit. The spectrum analyzer outputs current feedback for high-field detuning frequencies with a 4 MHz and 1 kHz sweep width.

During high-field imaging, the Feshbach bias magnetic field causes significant energy level splitting. Since the energy levels become resolvable after splitting, there is a closed transition for atomic imaging. Therefore, no repump light is needed. According to the Zeeman energy level splitting formula, at 832 Gauss (Feshbach resonance point), the imaging frequency for atoms in the $|1\rangle$ state is detuned by -1.234 GHz from the zero-field condition, and for atoms in the $|2\rangle$ state, it is detuned by -1.311 GHz from the zero-field condition. Since the beat frequency locking of the high-field imaging light is directly with the zero-field resonant light, it is convenient to obtain the appropriate imaging light based on this reference frequency and can also be used to verify the accuracy of the magnetic field.

Figure 3(b) shows an enlarged view of the beat frequency circuit. The laser stabilizes its frequency through beat frequency locking, with the frequency difference being the de-

tuning of the high-field imaging light. The two components of light enter the beat frequency photodetector (Newport 818-45-F) through a fiber coupling head. The resulting signal is amplified using a 40 dB RF amplifier (ZKL-1R5+), then passes through a custom-made directional coupler circuit (PDC-10-5+) before being input into a custom-made frequency and phase discriminator circuit. The selected chip ADF4007 can both divide and mix frequencies for frequency and phase discrimination. A 16 or 32 rate position is chosen in the circuit (determined by the magnetic field strength), meaning that the frequency signal is divided and compared with another custom-made reference source circuit (output frequency range 67.6–125 MHz) to obtain the beat frequency error signal. After adjusting the parameters of the custom ultrafast loop controller (Fast PID), the output signal is connected to the current modulation port of the semiconductor laser for corresponding frequency locking. Due to the broad linewidth of the ECDL and frequency drift of several hundred MHz when not locked, the traditional piezoelectric ceramic (PZT) modulation bandwidth is limited (10 kHz) and cannot narrow the linewidth, while high-field imaging requires a narrow linewidth. Therefore, we optimize to use current feedback with a larger modulation bandwidth (1 MHz). By employing fast PID locking, the linewidth can be narrowed to approximately 100 kHz. Figure 3(a) shows the sub-figure of the locking point at 740 Gauss (1.176 GHz) with a corresponding sweep width of 1 kHz, as well as the locking point after a 16-fold frequency division with a sweep width of 4 MHz.

4. High-field imaging analysis

4.1. Typical imaging results

We prepare a two-state mixture of lithium atoms in their lowest hyperfine states $|1\rangle = |F = 1/2, m_F = 1/2\rangle$ and $|2\rangle = |F = 1/2, m_F = -1/2\rangle$. Subsequently, we perform evaporative cooling in the optical dipole trap at 810 Gauss of the Feshbach resonance and switch to the BEC and BCS sides in our experiment. The detailed experimental setup has been described in our previous work.[26] In the experiment, by scanning the Feshbach magnetic field, one can study the formation process of molecules and the corresponding optical density distribution within the BEC–BCS crossover region.

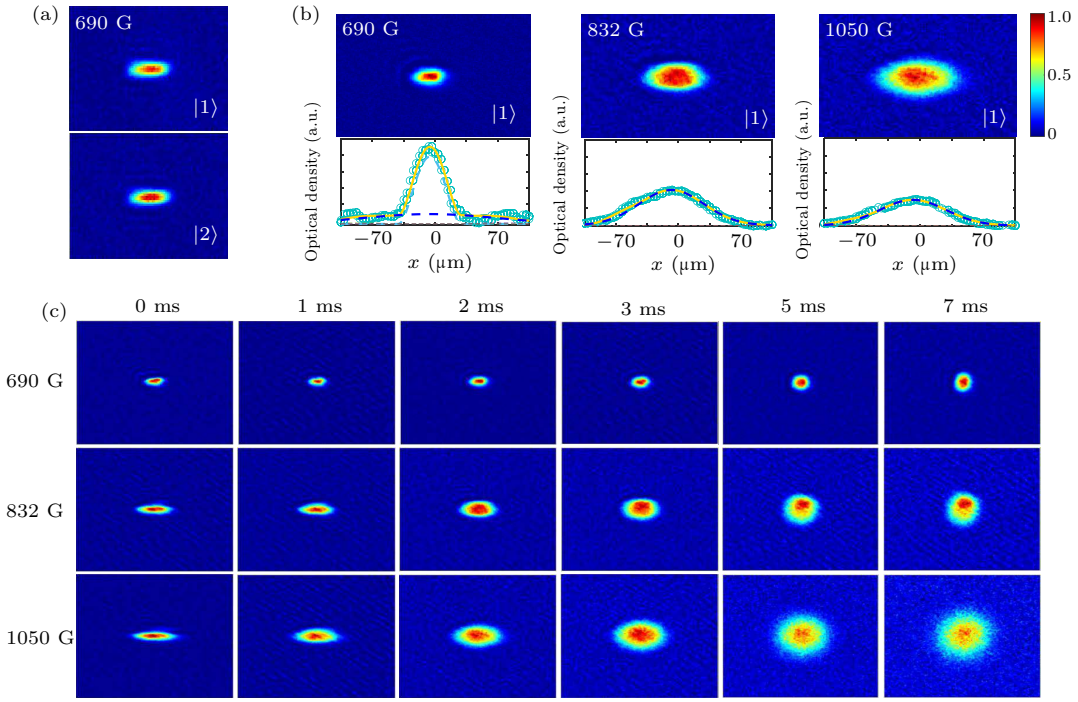


Fig. 4. Imaging results presentation. (a) Typical images of vertical direction absorption imaging for the $|1\rangle$ and $|2\rangle$ states at 690 Gauss. (b) Absorption imaging of the $|1\rangle$ state at different magnetic fields along with the corresponding axial optical density integrated curves. At $B = 690$ Gauss, the system is in the molecular Bose–Einstein condensate regime, where the yellow and blue lines represent the bi-modal fitting and the Gaussian fitting, respectively. At $B = 832$ Gauss, the system is in the unitary regime, where the density distribution is almost entirely fitted by a Gaussian function. At $B = 1050$ Gauss, the system corresponds to the BCS regime, where the density distribution is fitted by a Gaussian function. All images are results with $t_{\mathrm{TOF}} = 2$ ms. Green circles represent experimental data points. (c) Images of the three typical regions of BEC–BCS with different t_{TOF}.

Figure 4 presents a set of typical images for the BEC–BCS crossover. Figure 4(a) shows a typical contrast image of atoms in $|1\rangle$ and $|2\rangle$ under high-field vertical imaging at 690 Gauss, with corresponding frequencies of 1.032 GHz and 1.108 GHz, respectively. Absorption images are taken after the TOF process ($t_{\mathrm{TOF}} = 2$ ms) to measure the distribution of particles. Three typical images under different interactions are shown in Fig. 4(b). By integrating along the y-axis, we obtain the corresponding density distribution function of particles, as shown in the bottom panel of Fig. 4(b). Under the

condition of a magnetic field strength of 690 Gauss, the atoms exhibit a clear bimodal distribution, forming a molecular BEC. In the unitary and BCS regions, the atomic distribution is fitted with a Gaussian function. And here only the Gaussian function is used to reflect the impact of strong interactions and weak attractive interactions on the atomic density distribution. Figure 4(c) shows the absorption imaging of BEC–BCS with different t_{TOF}. It can be clearly seen from the figure that the aspect ratio of the atomic ensemble increases gradually with the TOF time under different interactions, which demonstrates the feasibility of the high-field imaging system design.

4.2. Probing light intensity fluctuations analysis

In this system, we employ a weak probe pulse ($0.1I_{\mathrm{sat}}$) and a short pulse duration (20 μs) to suppress the effects of Doppler shifts and random walks. Under these conditions, the OD can be approximated by the first term of Eq. (6) without the need to evaluate the value of I_{sat}.

Accurate determination of the atomic distribution is crucial, as parameters such as temperature, atom number, and density can be calculated from this information. However, in practice, certain noise signals limit the measurement accuracy, and in our experiment, fluctuations in the probe light intensity significantly interfere with the measurement of atom numbers under the background of uniform noise. Mainly, there is a time interval between the three images in absorption imaging.

As shown in Fig. 5(a), we observe two typical images with different brightness (dark and light) levels from 20 repeated measurements of atom-free imaging. We select two regions of image (ROIs) (yellow boxes) from each image to analyze the noise from light intensity fluctuations. Figure 5(b) displays the variation in the ratio of the average $\overline{OD}_{\mathrm{ROI}}$ of the selected atom-free regions to the $\sum OD$ of the entire image after 20 repeated measurements. The inset shows the variation of the $\sum OD$ in the selected atom-free regions and the entire image. Here, the blue star represents ROI 1, the brown diamond represents ROI 2, and the square represents the entire image. It can be seen from the pattern that although the ratio of the $\overline{OD}_{\mathrm{ROI}}$ in the selected regions to the $\sum OD$ changes slightly, the actual OD values in these regions are significantly affected by light intensity fluctuations and require further correction.

To correct for the effects of probe light intensity fluctuations, we first analyze the imaging in the atom-free region. The magnitude of light intensity fluctuations in the background noise I_{bg} is less than 10^{-2} compared to the other two images and can be neglected. Therefore, Eq. (6) can be modified as

$$\begin{aligned} OD' &= -\ln\left(\frac{I'_{\mathrm{f}}}{I'_{\mathrm{i}}}\right) = -\ln\left(\frac{I'_{\mathrm{atoms}}}{I'_{\mathrm{light}}}\right) = -\ln\left(\frac{cI_{\mathrm{atoms}}}{I_{\mathrm{light}}}\right) \\ &= -\ln(c) - \ln\left(\frac{I_{\mathrm{atoms}}}{I_{\mathrm{light}}}\right). \end{aligned} \tag{7}$$

Here, c is the proportionality coefficient for light intensity fluctuations. In practice, in the atom-free region of the imaging, $OD' = 0$. Therefore, according to Eq. (7), the value of c is obtained to correct the actual OD.

In the actual measurement, we select several image regions ROI_i that completely enclose all particles, with areas S_i, and obtain the summed OD values A_i within different regions. We perform a linear fit between A_i and S_i for different regions and calculate the proportionality coefficient c for correcting light intensity fluctuations using

$$\ln(c) = \frac{A_i - A_j}{S_i - S_j}. \tag{8}$$

Therefore, the actual OD value is given by

$$OD = OD' + \ln(c). \tag{9}$$

In our experiments, we apply this method to correct for the effects of probe light intensity fluctuations on actual OD measurements in the presence of atoms.[27] Figure 5(c) shows a typical image of the first-order momentum mode distribution of particles under strong interactions at 747 Gauss. We employ a shortcut lattice pulsing technique to populate discrete momentum states. For a lattice depth $V_0 = 10E_{\mathrm{r}}$, we apply a two-pulse sequence with timings $(t_1^{\mathrm{on}}, t_1^{\mathrm{off}}, t_2^{\mathrm{on}}, t_2^{\mathrm{off}}) = (12.3, 6.8, 7.1, 18.2)$ μs, achieving 99.9% theoretical fidelity in the non-interacting limit.[27,28] The 1D optical lattice, whose lattice constant $D = \lambda/2 = 532$ nm, is composed of a $\lambda = 1064$ nm laser beam and a retro-reflected beam. The characteristic lattice energy is $E_{\mathrm{r}} = \hbar^2 k^2/2m$, where $k = \pi/D$ and m is the mass of a lithium molecule ($^6\mathrm{Li}_2$). The yellow boxes are centered on the initial BEC position and enclose the first-order momentum mode distribution. We select different square regions, denoted as square areas S_i, and use the $\sum OD$ values A_i within these regions to statistically infer the particle numbers. Figure 5(d) displays the relationship between the $\sum OD$ values A_i and the corresponding areas S_i before and after correction. The star data in the blue dashed box represent the corrected results, which we magnify in the inset at the lower right corner. The circular data correspond to the uncorrected measurement results. It can be seen from the figure that, without correction, A_i increases with the increase in the selected region. However, the actual region containing atoms is limited to the first-order momentum mode region, indicating that light intensity fluctuations significantly affect the calculation of A_i. In contrast, after correction, A_i values remain essentially consistent across different regions, especially for small-area statistics, which become more accurate. Therefore, to enhance the reliability of data in actual measurements, we calculate the light intensity proportionality coefficient c for each image to correct for light intensity fluctuations and noise.

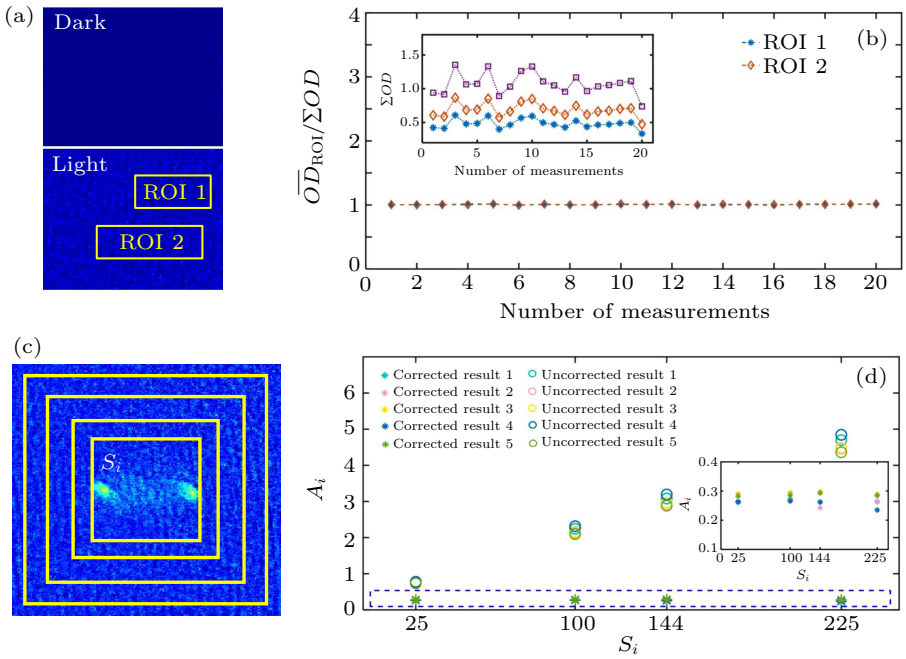


Fig. 5. (a) When imaging without atoms, two typical images with different brightness levels (dark and light) are shown, with two regions of image (yellow boxes) selected in each image. (b) In the atom-free region, the relationship between the number of repeated measurements and the ratio of $\overline{OD}_{\mathrm{ROI}}$ of the selected atom-free regions to the $\sum OD$ of the entire image is shown.The inset illustrates the relationship between the number of repeated measurements and the $\sum OD$. The blue star represents ROI 1, the brown diamond represents ROI 2, and the purple square represents the entire image. (c) In the presence of atoms, a typical image of the first-order momentum mode of particles at 747 Gauss is shown. Yellow boxes indicate different square regions S_i centered on the BEC position that enclose all particles. (d) In the presence of atoms, the relationship between the summed optical density A_i and the measurement area S_i in different regions is shown. The blue dashed box highlights the corrected results, with the inset providing a magnified view of the corrected data. Stars indicate the corrected measurement data, while circles represent the uncorrected measurement data.

5. Conclusion

In this work, we design a high-field imaging system with a large frequency range and good robustness, considering the energy level structure of ^{6}Li atoms. we adopt a frequency offset phase-locking method to obtain the probe light. This imaging system covers the entire crossover region from BEC–BCS and realizes free switching between zero-field and high-field imaging. In addition, we correct the light intensity of the absorption imaging by introducing a proportionality coefficient c in the calculation of optical density, avoiding the disturbance of light intensity fluctuation noise on the particle number statistics in the experiment and providing reliable data support for strong interaction experiments. In summary, this work not only offers insights into the design of absorption imaging systems for quantum gas experiments under strong magnetic fields but also provides a reference for the corresponding imaging analysis. While our method optimizes imaging performance in uniform background environments, extending it to non-uniform scenarios remains a future challenge.

Acknowledgements

Project supported by the National Natural Science Foundation of China (Grant Nos. 92365208 and 11920101004) and the National Key Research and Development Program of China (Grant Nos. 2021YFA0718300 and 2021YFA1400900).

Data availability statement

The data that support the findings of this study are openly available in Science Data Bank at https://doi.org/10.57760/sciencedb.j00113.00226.

References

[1] Giorgini S, Pitaevskii Lev P and Stringari S 2008 *Rev. Mod. Phys.* **80** 1215
[2] Bloch I, Dalibard J and Zwerger W 2008 *Rev. Mod. Phys.* **80** 885
[3] Anderson M H, Ensher J R, Matthews M R, Wieman C E and Cornell E A 1995 *Science* **269** 198
[4] Chin J K, Miller D E, Liu Y, Stan C, Setiawan W, Sanner C, Xu K and Ketterle W 2006 *Nature* **443** 961
[5] Guo X X, Yu Z C, Wei F S, Jin S J, Chen X Z, Li X P, Zhang X B and Zhou X J 2022 *Sci. Bull.* **67** 2291
[6] Hu D, Niu L X, Jin S J, Chen X Z, Dong G J, Schmiedmayer J and Zhou X J 2018 *Commun. Phys.* **1** 29
[7] Haim A, Henrik B and Preben B 2008 *Appl. Opt.* **47** 5354
[8] Niu L X, Guo X X, Zhan Y, Chen X Z, Liu W M and Zhou X J 2018 *Appl. Phys. Lett.* **113** 144103
[9] Smith D A, Aigner S, Hofferberth S, Gring M, Andersson M, Wildermuth S, Krüger P, Schneider S, Schumm T and Schmiedmayer J 2011 *Opt. Express* **19** 8471
[10] Chin C, Grimm R, Julienne P and Tiesinga E 2010 *Rev. Mod. Phys.* **82** 1225
[11] Svetlana K 2014 *Rep. Prog. Phys* **77** 093901
[12] Bourdel T, Khaykovich L, Cubizolles J, Zhang J, Chevy F, Teichmann M, Tarruell L, Kokkelmans S J J M F and Salomon C 2004 *Phys. Rev. Lett.* **93** 050401
[13] Jochim S, Bartenstein M, Altmeyer A, Hendl G, Riedl S, Chin C, Hecker D J and Grimm R 2003 *Science* **302** 2101
[14] Petrov D S, Salomon C and Shlyapnikov G V 2004 *Phys. Rev. Lett.* **93** 090404
[15] Zwierlein M W, Stan C A, Schunck C H, Raupach S M F, Kerman A J and Ketterle W 2004 *Phys. Rev. Lett.* **92** 120403

[16] Zhang Z D, Yao K X, Feng L, Hu J Z and Chin C 2020 *Nat. Phys.* **16** 652

[17] Liu Y Q, Zhang Z C, Miao S W, Zhao Z H, Wang H C, Chen W L and Hu J Z 2023 *Phys. Rev. Appl.* **20** 014037

[18] Hueck K, Luick N, Sobirey L, Siegl J, Lompe T, Moritz H, Clark L W and Chin C 2017 *Opt. Express* **25** 8670

[19] Horikoshi M, Ito A, Ikemachi T, Aratake Y, Kuwata-Gonokami M and Koashi M 2017 *J. Phys. Soc. Jpn.* **86** 104301

[20] Wang D, Neyenhuis B, De Miranda M H G, Ni K-K, Ospelkaus S, Jin D S and Ye J 2010 *Phys. Rev. A* **81** 061404

[21] Hans M, Schmutte F, Viermann C, Liebster N, Sparn M, Oberthaler M K and Strobel H 2021 *Rev. Sci. Instrum.* **92** 023203

[22] Vibel T, Christensen M B, Kristensen M A, Thuesen J J, Stokholm L N, Weidner C A and Arlt J J 2024 *J. Phys. B: At. Mol. Opt. Phys.* **57** 145301

[23] Reinaudi G, Lahaye T, Wang Z and Guéry-Odelin D 2007 *Opt. Lett.* **32** 3143

[24] Mao D k, Shui H M, Yin G L, Peng P, Wang C W and Zhou X J 2024 *Chin. Phys. B* **33** 024209

[25] Puentes G 2012 *Appl. Phys. B* **107** 11

[26] Wei F S, Zhang Z X, Chen Y Y, Shui H M, Liang Y, Li C and Zhou X J 2024 *Phys. Rev. A* **109** 043313

[27] Chen Y Y, Zhang Z X, Lai C K, Shui H M, Liang Y, Wei F S and Zhou X J 2025 *Phys. Rev. A* **111** 043303

[28] Zhou X, Jin S and Schmiedmayer J 2018 *New J. Phys.* **20** 055005